



Title	Effect of lattice distortions on the electron and thermal transport properties of transparent oxide semiconductor Ba _{1-x} Sr _x SnO ₃ solid solution films
Author(s)	Cho, Hai Jun; Sato, Koichi; Wei, Mian; Kim, Gowoon; Ohta, Hiromichi
Citation	Journal of Applied Physics, 127(11), 115701 https://doi.org/10.1063/5.0002172
Issue Date	2020-03-21
Doc URL	http://hdl.handle.net/2115/80627
Rights	This article may be downloaded for personal use only. Any other use requires prior permission of the author and AIP Publishing. This article appeared in Cho Hai Jun, Sato Koichi, Wei Mian, Kim, Gowoon, Ohta, Hiromichi. Effect of lattice distortions on the electron and thermal transport properties of transparent oxide semiconductor Ba _{1-x} Sr _x SnO ₃ solid solution films. Journal of Applied Physics, 127(11), 115701, 2020 and may be found at https://doi.org/10.1063/5.0002172 .
Type	article
File Information	5.0002172.pdf



[Instructions for use](#)

Effect of lattice distortions on the electron and thermal transport properties of transparent oxide semiconductor $\text{Ba}_{1-x}\text{Sr}_x\text{SnO}_3$ solid solution films

Cite as: J. Appl. Phys. **127**, 115701 (2020); <https://doi.org/10.1063/5.0002172>

Submitted: 22 January 2020 . Accepted: 25 February 2020 . Published Online: 17 March 2020

Hai Jun Cho , Koichi Sato, Mian Wei , Gowoon Kim , and Hiromichi Ohta 

COLLECTIONS

 This paper was selected as an Editor's Pick



View Online



Export Citation



CrossMark

ARTICLES YOU MAY BE INTERESTED IN

[Tunable hierarchical wrinkling: From models to applications](#)

Journal of Applied Physics **127**, 111101 (2020); <https://doi.org/10.1063/1.5143651>

[High electrical conducting deep-ultraviolet-transparent oxide semiconductor La-doped \$\text{SrSnO}_3\$ exceeding \$\sim 3000 \text{ S cm}^{-1}\$](#)

Applied Physics Letters **116**, 022103 (2020); <https://doi.org/10.1063/1.5128410>

[Landau-Devonshire derived phase diagram of the \$\text{BiFeO}_3\$ — \$\text{PbTiO}_3\$ solid solution](#)

Journal of Applied Physics **127**, 104102 (2020); <https://doi.org/10.1063/1.5144151>

Lock-in Amplifiers
up to 600 MHz



Watch



Effect of lattice distortions on the electron and thermal transport properties of transparent oxide semiconductor $\text{Ba}_{1-x}\text{Sr}_x\text{SnO}_3$ solid solution films



Cite as: J. Appl. Phys. 127, 115701 (2020); doi: 10.1063/5.0002172

Submitted: 22 January 2020 · Accepted: 25 February 2020 ·

Published Online: 17 March 2020



View Online



Export Citation



CrossMark

Hai Jun Cho,^{1,2,a)} Koichi Sato,² Mian Wei,² Gowoon Kim,² and Hiromichi Ohta^{1,2,a)}

AFFILIATIONS

¹Research Institute for Electronic Science, Hokkaido University, N20W10, Sapporo 001-0020, Japan

²Graduate School of Information Science and Engineering, Hokkaido University, N14W9, Kita, Sapporo 060-0814, Japan

^{a)}Authors to whom correspondence should be addressed: joon@es.hokudai.ac.jp and hiromichi.ohta@es.hokudai.ac.jp

ABSTRACT

La-doped ASnO_3 ($A = \text{Ba}$ and Sr) have great potential as advanced transparent oxide semiconductors due to their large optical bandgap and relatively high electron mobility. The bandgap of $\text{Ba}_{1-x}\text{Sr}_x\text{SnO}_3$ solid solution increases from 3.2 eV (BaSnO_3) to 4.6 eV (SrSnO_3) with x . However, the increase in the bandgap is accompanied by reductions in the electrical conductivity. The versatility in the changes in the electrical properties is not trivial, and property optimization has been challenging. Here, we propose a simple metric for quantifying the transport properties of ASnO_3 . We investigated the electron/thermal transport properties of $\text{Ba}_{1-x}\text{Sr}_x\text{SnO}_3$ solid solution films and their relationship with the lattice distortion. The results suggest that all the transport properties of $\text{Ba}_{1-x}\text{Sr}_x\text{SnO}_3$ are dominated by the lattice distortion. This phenomenon is attributed to the distortions in the SnO_6 octahedron, which consists of the conduction band.

Published under license by AIP Publishing. <https://doi.org/10.1063/5.0002172>

I. INTRODUCTION

Transport properties of perovskite stannate (ASnO_3 , $A = \text{Ba}$ and Sr) are of great interest in advanced transparent oxide semiconductor technologies.^{1,2} The edge-sharing SnO_6 octahedra provide a highly dispersive conduction band that consists of Sn 5s orbitals with a small carrier effective mass (m^*),^{2,3} and the A-site elements can change the optical bandgap.⁴ For these reasons, the optoelectronic properties of ASnO_3 are highly versatile. For example, n-type BaSnO_3 has a cubic structure with an effective mass of $\sim 0.4 m_e$ and an optical bandgap of ~ 3.2 eV.^{3–5} Its single crystal exhibits an excellent carrier electron mobility (μ) of ~ 320 $\text{cm}^{-2} \text{V}^{-1} \text{s}^{-1}$ at room temperature, which is comparable to classical semiconductors.¹ On the other hand, if Ba is replaced with Sr (SrSnO_3), the effective mass reduces to $\sim 0.2 m_e$, while the optical bandgap increases to ~ 4.6 eV.⁶ This bandgap can sufficiently transmit deep-UV light (>4.1 eV), which is crucial for DNA sensing.⁷ However, despite the smaller m^* , the carrier electron mobility of n-type SrSnO_3 are significantly lower than those of n-type BaSnO_3 ,^{6,8–12} which is interesting since the conduction bands of both these materials consist of SnO_6 octahedra.

The suppression of carrier electron mobility observed from BaSnO_3 ($\mu \sim 320$ $\text{cm}^{-2} \text{V}^{-1} \text{s}^{-1}$) \rightarrow SrSnO_3 ($\mu \sim 60$ $\text{cm}^{-2} \text{V}^{-1} \text{s}^{-1}$)^{6,12} implies that substituting Sr for Ba greatly reduces the mean free path of electrons in ASnO_3 . The main scattering mechanism remains unclear but is likely related to the crystallographic transformation from cubic (BaSnO_3 ¹³) to orthorhombic (SrSnO_3 ¹⁴) structure (Fig. 1), as the SnO_6 octahedron will be severely distorted. This will also strongly affect vibrational properties such as thermal conductivity. In this regard, clarifying the effect of substituting Sr for Ba in BaSnO_3 on the evolution of both electron and thermal transport properties as well as lattice distortion is crucial for understanding the physical properties of ASnO_3 and controlling their properties for device applications.

In this study, we investigated the effect of lattice distortion on the electron and thermal transport properties of $\text{Ba}_{1-x}\text{Sr}_x\text{SnO}_3$ solid solution films. Undoped $\text{Ba}_{1-x}\text{Sr}_x\text{SnO}_3$ solid solution films were used for thermal conductivity measurements, whereas 3% La-doped solid solution [$\text{La}_{0.03}(\text{Ba}_{1-x}\text{Sr}_x)_{0.97}\text{SnO}_3$] films were used for electron transport property measurements. Thick films

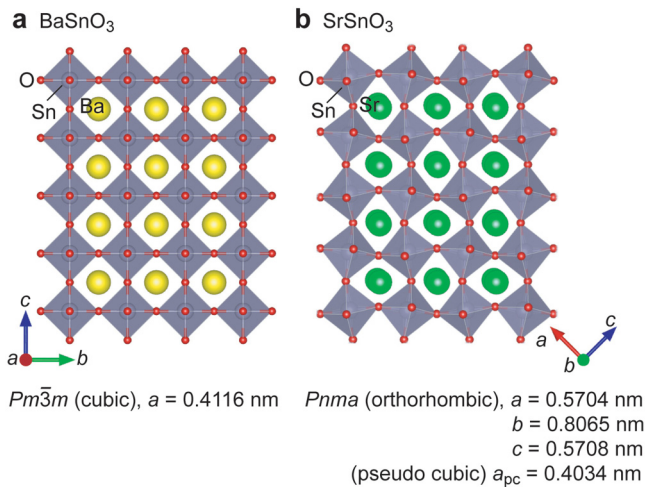


FIG. 1. Schematic crystal structure of (a) BaSnO₃ and (b) SrSnO₃. SnO₆ octahedra are aligned in the case of BaSnO₃ but those of SrSnO₃ are not. The lattice parameter of cubic BaSnO₃ (a) is 0.4116 nm and that of pseudo-cubic SrSnO₃ (a_{pc}) is 0.4034 nm.¹⁴

(thickness: ~ 300 nm) were used to relax the strains from the lattice mismatch at the film/substrate interface.¹⁵ The Sr content x in the solid solution was varied from 0 to 1, and the data analysis was performed with a strong emphasis on establishing a relationship between the transport properties and lattice distortion. Crystallographic characterizations showed that the substitution of an A-site ion strongly increases the deviation from a cubic structure. This overwhelms the dopant scatterings from the A-site substitution and dominates the changes in the electron transport properties. Thermal conductivity usually decreases with increasing atomic mass.¹⁶ However, although Sr (87.62 amu) is lighter than Ba (137.33 amu), the thermal conductivity of SrSnO₃ was much lower than that of BaSnO₃, confirming all transport properties are dominated by the deviation from a cubic phase. These contributions reveal a fundamental factor that affects the transport properties in ASnO₃, which are of significant importance for engineering their transport properties in various applications.

II. EXPERIMENTAL

Undoped and 3% La-doped Ba_{1-x}Sr_xSnO₃ solid solution films were heteroepitaxially grown on SrTiO₃ (001) substrates using pulsed laser deposition (KrF excimer laser, ~ 2 J cm⁻² pulse⁻¹, 10 Hz). The substrate temperature and oxygen pressure were kept at 800 °C and 10 Pa during the film growth, respectively. The thicknesses of all films were ~ 300 nm, which relaxes the strain coming from the lattice mismatch between the film and the substrate. Out-of-plane x-ray Bragg diffraction patterns and reciprocal space mappings (RSMs) were measured with a high-resolution x-ray diffraction (XRD, Cu K α_1 , ATX-G, Rigaku Co.) equipment. The lateral grain size (D) of the films was evaluated from the coherence lengths of the diffraction peaks in the RSMs. The powder XRD patterns of the solid solution

targets were also measured, and the XRD patterns were analyzed with Rietveld refinement using the Rietan 2000 program.¹⁷

The thermal conductivity (κ) of the undoped Ba_{1-x}Sr_xSnO₃ films in the out-of-plane direction was measured using time-domain thermo-reflectance (TDTR, PicoTR, PicoTherm Co.) at room temperature. To prevent the surface roughness from affecting the TDTR signal, the films were annealed in air at 1400 °C for ~ 15 min to obtain stepped and terraced surfaces (Fig. S1 in the [supplementary material](#)). The electrical conductivity (σ), Hall mobility (μ_{Hall}), and carrier concentration (n) of the La-doped La_{0.03}(Ba_{1-x}Sr_x)_{0.97}SnO₃ films were measured in the in-plane direction at room temperature. The Hall voltage was measured using the conventional d.c. four-probe method with the van der Pauw electrode configuration. The thermopower (S) of the films was measured in the in-plane direction by creating a temperature difference between two edges of the film. Details on our S measurement is available elsewhere.⁴

III. RESULTS AND DISCUSSION

Figure 2 summarizes the XRD crystallographic analyses. Only intense diffraction peaks of $00l_{pc}$ of Ba_{1-x}Sr_xSnO₃ solid solution films are seen together with $00l$ SrTiO₃ substrate in the out-of-plane XRD patterns ($x = 0, 0.3, 0.6,$ and 0.9) [**Fig. 2(a)**]. Note that the XRD characterizations of orthorhombic structure (i.e., SrSnO₃) represent a pseudo-cubic unit cell that consists of basis atoms. For example, the pseudo-cubic unit cell of SrSnO₃ has Sr $\times 1$, Sn $\times 1$, and O $\times 3$. The scattering vector shifts to the right with increasing x , which indicates a reduction in the pseudo-cubic lattice parameter in the out-of-plane direction. In order to measure the film thickness, we used Pendellösung fringes [**Fig. 2(b)**]. **Figure 2(c)** shows a typical RSM of the Ba_{0.7}Sr_{0.3}SnO₃ solid solution film around (-103) SrTiO₃. The lattice parameter in the out-of-plane direction (c -axis) was 0.41043 nm and that in the in-plane direction (a -axis) was 0.40853 nm, respectively. The lateral grain size (D) can be calculated as $(\text{integral width})^{-1}$ in the in-plane Bragg diffraction pattern. The RSMs of all films can be found in Figs. S2 and S3 in the [supplementary material](#).

Figure 3 shows changes in κ of the undoped Ba_{1-x}Sr_xSnO₃ solid solution films as a function of x . At $x = 0$ (BaSnO₃), κ is the highest (8 W m⁻¹ K⁻¹). This value monotonically decreases to ~ 2.8 W m⁻¹ K⁻¹ at $x = 0.7$. As x approaches 1, the κ increases to 4.4 W m⁻¹ K⁻¹. The κ of Ba_{1-x}Sr_xSnO₃ solid solution films exhibit a concavity and goes through a phase transition from the BaSnO₃ dominated phase to the SrSnO₃ dominated phase somewhere near $x \sim 0.7$. This type of behavior is commonly observed in solid solution systems¹⁸⁻²⁰ due to the scattering from dopants, but κ of the Ba_{1-x}Sr_xSnO₃ system is a bit different from that of conventional solid solutions. In conventional material systems, heavier atoms usually suppress lattice vibrations and decrease κ .¹⁶ However, the κ of SrSnO₃ (Sr = 87.62 amu) is lower than that of BaSnO₃ (Ba = 137.33 amu). This suggests that the κ of Ba_{1-x}Sr_xSnO₃ solid solution films is dominated by a different factor.

Figure 4 summarizes the electron transport properties of 3% La-doped Ba_{1-x}Sr_xSnO₃ solid solution films as a function of x . The μ_{Hall} initially decreases from $x = 0$ (59 cm² V⁻¹ s⁻¹) to $x = 0.2$ (29 cm² V⁻¹ s⁻¹) and plateaus until $x = 0.4$ [**Fig. 4(b)**]. Then, the

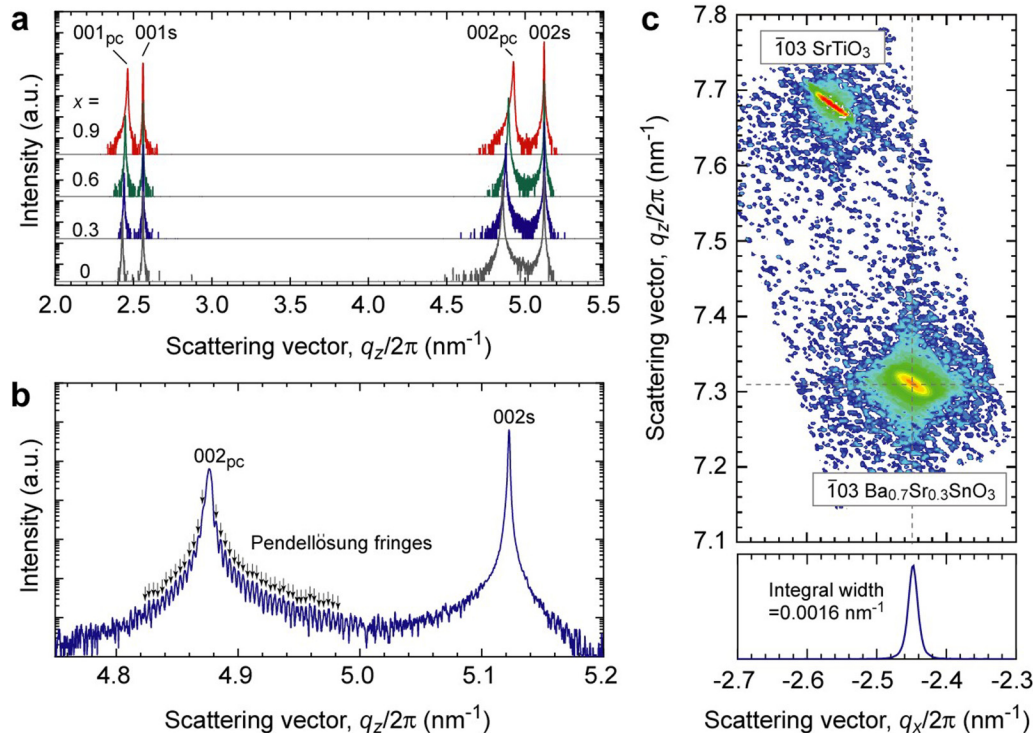


FIG. 2. Crystallographic analyses. (a) Typical out-of-plane XRD patterns of undoped $\text{Ba}_{1-x}\text{Sr}_x\text{SnO}_3$ solid solution films ($x = 0, 0.3, 0.6,$ and 0.9). Only intense diffraction peaks of 00_{pc} of $\text{Ba}_{1-x}\text{Sr}_x\text{SnO}_3$ solid solution are seen together with the $00/\text{SrTiO}_3$ substrate. The scattering vector shifts to the right with increasing x , which indicates a reduction in the pseudo-cubic lattice parameter in the out-of-plane direction. (b) Magnified XRD pattern of the $\text{Ba}_{0.7}\text{Sr}_{0.3}\text{SnO}_3$ solid solution film. Pendellösung fringes are clearly seen. The film thickness can be measured using the Pendellösung fringes. (c) X-ray reciprocal space mapping (RSM) of the $\text{Ba}_{0.7}\text{Sr}_{0.3}\text{SnO}_3$ solid solution film around 103 SrTiO_3 . The lattice parameter in the out-of-plane direction (c -axis) is 0.41043 nm and that in the in-plane direction (a -axis) is 0.40853 nm , respectively. The lateral grain size (D) can be calculated as $(\text{integral width})^{-1}$ in the in-plane Bragg diffraction pattern.

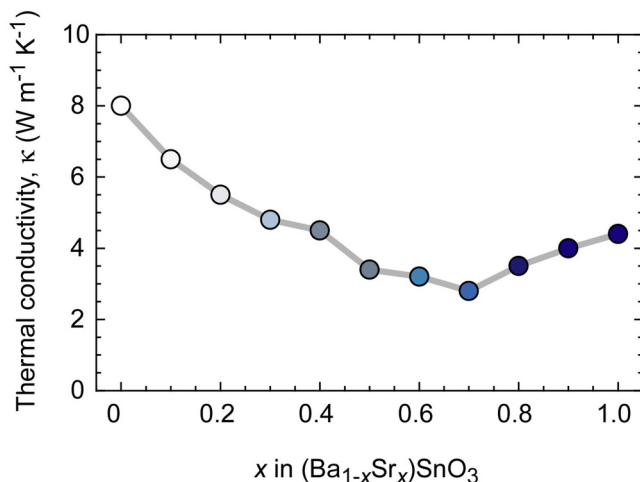


FIG. 3. Room temperature thermal conductivity of $\text{Ba}_{1-x}\text{Sr}_x\text{SnO}_3$ solid solution films in the out-of-plane direction.

μ_{Hall} suddenly drops at $x = 0.5$ ($12 \text{ cm}^2 \text{V}^{-1} \text{s}^{-1}$) and slowly decreases until $x = 0.8$ ($6 \text{ cm}^2 \text{V}^{-1} \text{s}^{-1}$). As x approaches from 0.8 to 1, the μ_{Hall} slowly increases up to $18 \text{ cm}^2 \text{V}^{-1} \text{s}^{-1}$. The other electrical transport properties (σ , n) exhibit similar behaviors [Figs. 4(a) and 4(c)], and the magnitude of the thermopower (S) increases with decreasing n [Fig. 4(c)]. While the A -site substitution increases dopant scatterings, the changes observed in the electron transport properties are too versatile to be explained by the dopant scattering alone. The electron transport properties were not proportional to the lateral grain sizes D [Fig. 4 and Fig. S4(b) in the supplementary material]. This suggests that the carrier electron mobilities are not limited by the grain boundaries. Similar to thermal conductivity, this suggests that the electron transport properties of La -doped $\text{Ba}_{1-x}\text{Sr}_x\text{SnO}_3$ solid solution films are controlled by a different factor.

Since BaSnO_3 and SrSnO_3 have different crystal structures, identifying changes in the lattice parameters is also crucial. Figure 5 shows the lattice parameters of the undoped and La -doped $\text{Ba}_{1-x}\text{Sr}_x\text{SnO}_3$ solid solution films. The dotted lines in Figs. 5(a) and 5(c) are linear regressions from the lattice parameter of BaSnO_3 (0.4116 nm) to that of SrSnO_3 (0.4034 nm). The lattice

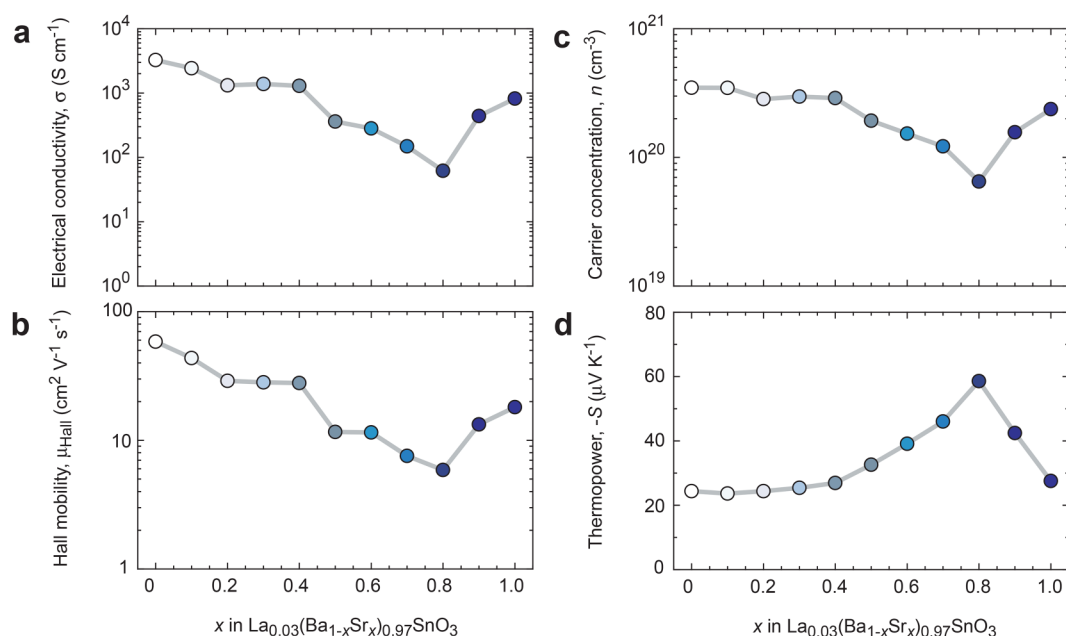


FIG. 4. Electron transport properties of La-doped Ba_{1-x}Sr_xSnO₃ solid solution films. (a) Electrical conductivity (σ), (b) Hall mobility (μ_{Hall}), (c) carrier concentration (n), and (d) thermopower (S). When $x \leq 0.8$, both μ_{Hall} and n decrease with x . Inflection points are located at $x = 0.8$ in all cases.

parameter in the in-plane direction is defined as the a -axis and that in the out-of-plane direction is defined as the c -axis. Both the a -axis and c -axis lattice parameters of undoped BaSnO₃ film are close to the bulk value, which indicates that the strain from the film/substrate interface is relaxed as we expected. Positive bowing is seen in the c -axis, whereas negative bowing is seen in the a -axis, showing that the a -axis is in compression while the c -axis is in tension. The lattice distortion is defined as $(c/a - 1) \times 100$ (%). The lattice distortion of the films maximizes at $x = 0.7$ – 0.8 .

There are several possibilities of the origin of the lattice distortion. Since the lattice mismatch between the film and the substrate decreases with x , the contribution of epitaxial strain would increase. However, the in-plane lattice parameter of the resultant films was always larger than that of the substrate. This shows that the epitaxial strain does not dominate the lattice distortion. In order to clarify the dominant origin of the lattice distortion, we performed the Rietveld analyses of the powder diffraction patterns of the Ba_{1-x}Sr_xSnO₃ PLD target ceramics. We found that the space group of $x \leq 0.5$ is $Pm\bar{3}m$ (cubic perovskite), whereas $x \geq 0.7$ is $Pnma$ (orthorhombic perovskite) (Fig. S5 in the [supplementary material](#)). The crystal structures drawn from the Rietveld analysis results also demonstrate that the lattice distortion at $x = 0.7$ is much greater than that at $x = 1$ (Fig. S6 in the [supplementary material](#)). These results would indicate that the lattice distortion is spontaneously introduced due to the stability of orthorhombic symmetry around $x \sim 0.7$.

Interestingly, the changes observed in the lattice distortion are similar with those observed from the electron and thermal transport properties. In the undoped Ba_{1-x}Sr_xSnO₃ solid solution

system, BaSnO₃ ($x = 0$) initially exhibits a near-perfect cubic structure, where the κ is the highest ($8 \text{ W m}^{-1} \text{ K}^{-1}$). The lattice distortion gradually increases until $x = 0.7$, where the κ exhibits a minimum [Figs. 3 and 5(b)]. As x increases further, the lattice distortion gradually reduces until $x = 1$ (SrSnO₃). Since the bowing of lattice parameters occurred in the BaSnO₃–SrSnO₃ solid solution system like the BaTiO₃–SrTiO₃ system,²¹ the lattice distortion was maximized around $x = 0.7$, and the cubic structure is not fully recovered, which is consistent with the κ of SrSnO₃ being lower than that of BaSnO₃. In the case of La-doped Ba_{1-x}Sr_xSnO₃ solid solution films, the lattice distortion has an increasing tendency until $x = 0.8$ and decreases as it approaches $x = 1$, which is consistent with all electron transport properties [Figs. 4 and 5(d)]. However, unlike the lattice distortion, a plateau can be seen in μ_{Hall} and n from $x = 0.2$ to 0.4 . This plateau implies that the dopant scatterings from the A-site substitution are not significant but not trivial to understand. It seems that $\sim 0.6\%$ is a critical distortion in SnO₆ for the electron transport properties of ASnO₃. For example, a sudden drop in μ_{Hall} and n is observed at $x = 0.5$ when the lattice distortion reaches $\sim 0.7\%$. In addition, an abrupt jump is observed in μ_{Hall} and n at $x = 0.9$ when the lattice distortion reduces to $\sim 0.5\%$. However, we would like to note that the lattice distortions from $x = 0.2$ to 0.4 are within the uncertainty (0.1%), and the actual lattice distortion in this region may be similar. Compared to the undoped Ba_{1-x}Sr_xSnO₃ solid solution films, which exhibited a transition at $x = 0.7$, the transition in the La-doped Ba_{1-x}Sr_xSnO₃ solid solution films occurs a bit later ($x = 0.8$). This is likely attributed to the extra distortions in the La-doped Ba_{1-x}Sr_xSnO₃ solid solutions from the La-dopants. In fact, the La-doped

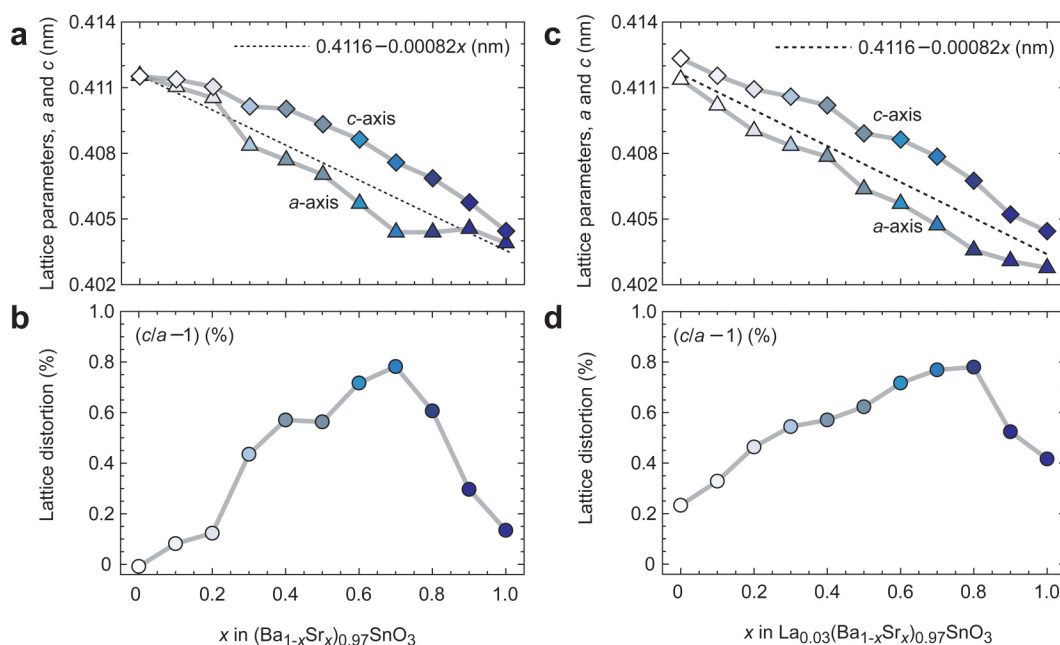


FIG. 5. Lattice parameters of undoped and La-doped $\text{Ba}_{1-x}\text{Sr}_x\text{SnO}_3$ solid solution films. (a) Lattice parameters and (b) lattice distortion of undoped $\text{Ba}_{1-x}\text{Sr}_x\text{SnO}_3$ films. (c) Lattice parameters and (d) lattice distortion of La-doped $\text{Ba}_{1-x}\text{Sr}_x\text{SnO}_3$ films. The dotted lines in (a) and (c) are linear regressions from the lattice parameter of BaSnO_3 (0.4116 nm) to that of SrSnO_3 (0.4034 nm). The lattice parameter in the in-plane direction is defined as the a -axis and that in the out-of-plane direction is defined as the c -axis. Positive bowing is seen in the c -axis, whereas negative bowing is seen in the a -axis. The lattice distortion is defined as $(c/a - 1) \times 100$ (%). The changes in the transport properties are consistent with the changes in the lattice distortions.

$\text{Ba}_{1-x}\text{Sr}_x\text{SnO}_3$ solid solution films exhibit greater structural distortions compared to undoped $\text{Ba}_{1-x}\text{Sr}_x\text{SnO}_3$ solid solutions near $x = 0$ and $x = 1$ [Figs. 5(b) and 5(d)].

Since the propagation of vibrational waves is strongly affected by anharmonicity and strains in the lattice,²² the relationship between the lattice distortion and the κ of $\text{Ba}_{1-x}\text{Sr}_x\text{SnO}_3$ system is not surprising. While the changes in the κ of $\text{Ba}_{1-x}\text{Sr}_x\text{SnO}_3$ solid solution films are overall consistent with the changes observed from the lattice distortions [Fig. 2(c)], dopant scatterings also seem to play a minor role. For instance, the reduction of κ from $x = 0$ to 0.2 is likely attributed to the dopant scattering since the lattice distortion in this region is not significant [Fig. 2(c)]. In other regions, the location of the lowest κ and the highest lattice distortion ($x = 0.7$) suggests that the effect of lattice strain is stronger. Regarding the electron transport properties, the effect of lattice distortion demonstrates the relationship between anharmonicity and the electron scattering cross sections. However, the evolution of n is not straightforward. Since the optical bandgap of SrSnO_3 (~ 4.6 eV) is greater than that of BaSnO_3 (~ 3.2 eV), reduction in the La-dopant activation with the substitution of Sr is expected, but the n is not monotonic with the substitution of Sr. Figures 4(b) and 5(d) suggest that n is also controlled by the lattice distortion. This can be related to the strain-defect coupling in oxides.^{23–26} The lattice distortion creates linear strains along the axis. This can promote the formation of defects that create defect levels and suppress the activation of dopants.²⁷ These results demonstrate that

the electron and thermal transport properties of perovskite ASnO_3 are dominated by the lattice distortion, and maintaining the symmetry of SnO_6 octahedron is the key for preserving their transport properties.

IV. SUMMARY

In summary, we investigated the effect of lattice distortion on the electron and thermal transport properties of $\text{Ba}_{1-x}\text{Sr}_x\text{SnO}_3$ solid solution films. The thermal conductivity of $\text{Ba}_{1-x}\text{Sr}_x\text{SnO}_3$ monotonically decreases from $x = 0$ to 0.7 and then again monotonically increases until $x = 1$. For $x \geq 0.2$, the changes in the thermal conductivity are attributed to the scatterings from Sr substitution. However, in other regions, the lattice distortion of SnO_6 octahedron played a greater role again. The electron transport properties exhibited a decreasing tendency from $x = 0$ to 0.8 and then increased until $x = 1$. The changes in the carrier concentrations and carrier electron mobility were highly consistent with the evolution of lattice distortions, whereas the scattering from A -site substitutions were not significant. Maintaining the symmetry of the SnO_6 octahedron was a crucial factor for obtaining high electron transport properties in this system. The results of this study clarify the importance of SnO_6 octahedron in the transport properties of ASnO_3 , which will be valuable for unlocking their potential for device applications.

SUPPLEMENTARY MATERIAL

See the [supplementary material](#) for the topographic AFM images of the films, RSMs, lateral grain size, and Rietveld refinement results.

ACKNOWLEDGMENTS

This research was supported by Grants-in-Aid for Innovative Areas (No. 19H05791) from the JSPS. H.J.C. acknowledges the support from Nippon Sheet Glass Foundation for Materials Science and Engineering. H.O. acknowledges the support by Grants-in-Aid for Scientific Research A (No. 17H01314) from JSPS, the Asahi Glass Foundation, and the Mitsubishi Foundation. A part of this work was supported by the Dynamic Alliance for Open Innovation Bridging Human, Environment and Materials as well as the Network Joint Research Center for Materials and Devices. Student aids from the Asahi Glass Foundation (G. Kim) and the China Scholarships Council (M. Wei, No. 201808050081) are also greatly appreciated.

REFERENCES

- ¹H. J. Kim, U. Kim, H. M. Kim, T. H. Kim, H. S. Mun, B. G. Jeon, K. T. Hong, W. J. Lee, C. Ju, K. H. Kim, and K. Char, *Appl. Phys. Express* **5**, 061102 (2012).
- ²H. J. Kim, U. Kim, T. H. Kim, J. Kim, H. M. Kim, B. G. Jeon, W. J. Lee, H. S. Mun, K. T. Hong, J. Yu, K. Char, and K. H. Kim, *Phys. Rev. B* **86**, 165205 (2012).
- ³A. V. Sanchela, T. Onozato, B. Feng, Y. Ikuhara, and H. Ohta, *Phys. Rev. Mater.* **1**, 034603 (2017).
- ⁴A. V. Sanchela, M. Wei, H. J. Cho, and H. Ohta, *Small* **15**, 1805394 (2019).
- ⁵B. Hadjarab, A. Bouguelia, and M. Trari, *J. Phys. D Appl. Phys.* **40**, 5833 (2007).
- ⁶M. Wei, A. Sanchela, B. Feng, Y. Ikuhara, H. J. Cho, and H. Ohta, *Appl. Phys. Lett.* **116**, 022103 (2020).
- ⁷A. V. Tataurov, Y. You, and R. Owczarzy, *Biophys. Chem.* **133**, 66 (2008).
- ⁸H. Paik, Z. Chen, E. Lochocki, H. A. Seidner, A. Verma, N. Tanen, J. Park, M. Uchida, S. L. Shang, B. C. Zhou, M. Brutzam, R. Uecker, Z. K. Liu, D. Jena, K. M. Shen, D. A. Muller, and D. G. Schlom, *APL Mater.* **5**, 116107 (2017).
- ⁹S. Raghavan, T. Schumann, H. Kim, J. Y. Zhang, T. A. Cain, and S. Stemmer, *APL Mater.* **4**, 016106 (2016).
- ¹⁰A. Prakash, P. Xu, A. Faghaninia, S. Shukla, J. W. Ager, C. S. Lo, and B. Jalan, *Nat. Commun.* **8**, 15167 (2017).
- ¹¹A. V. Sanchela, M. Wei, J. Lee, G. Kim, H. Jeon, B. Feng, Y. Ikuhara, H. J. Cho, and H. Ohta, *J. Mater. Chem. C* **7**, 5797 (2019).
- ¹²T. Truttmann, A. Prakash, J. Yue, T. E. Mates, and B. Jalan, *Appl. Phys. Lett.* **115**, 152103 (2019).
- ¹³H. Mizoguchi, H. W. Eng, and P. M. Woodward, *Int. J. Inorg. Mater.* **43**, 1667 (2004).
- ¹⁴M. A. Green, K. Prassides, P. Day, and D. A. Neumann, *Int. J. Inorg. Mater.* **2**, 35 (2000).
- ¹⁵A. V. Sanchela, M. Wei, H. Zensyo, B. Feng, J. Lee, G. Kim, H. Jeon, Y. Ikuhara, and H. Ohta, *Appl. Phys. Lett.* **112**, 232102 (2018).
- ¹⁶H. J. Cho, Y. Takashima, Y. Nezu, T. Onozato, and H. Ohta, *Adv. Mater. Interfaces* **7**, 1901816 (2019).
- ¹⁷F. Izumi and T. Ikeda, *Mater. Sci. Forum* **321–324**, 198 (2000).
- ¹⁸B. Abeles, D. S. Beers, G. D. Cody, and J. P. Dismukes, *Phys. Rev.* **125**, 44 (1962).
- ¹⁹B. C. Daly, H. J. Maris, A. V. Nurmikko, M. Kuball, and J. Han, *J. Appl. Phys.* **92**, 3820 (2002).
- ²⁰M. Yasukawa and N. Murayama, *J. Mater. Sci. Lett.* **16**, 1731 (1997).
- ²¹G. S. Wang, Y. Y. ZHANG, C. L. Mao, and X. L. Dong, *Appl. Phys. Lett.* **91**, 061104 (2007).
- ²²H. J. Cho, B. Feng, T. Onozato, M. Wei, A. V. Sanchela, Y. Ikuhara, and H. Ohta, *Phys. Rev. Mater.* **3**, 094601 (2019).
- ²³A. Herklotz, D. Lee, E.-J. Guo, T. L. Meyer, J. R. Petrie, and H. N. Lee, *J. Phys. Condens. Matter* **29**, 493001 (2017).
- ²⁴U. Aschauer, R. Pfenninger, S. M. Selbach, T. Grande, and N. A. Spaldin, *Phys. Rev. B* **88**, 054111 (2013).
- ²⁵U. Aschauer, N. Vonruti, and N. A. Spaldin, *Phys. Rev. B* **92**, 054103 (2015).
- ²⁶J. Xi, H. Xu, Y. Zhang, and W. J. Weber, *Phys. Chem. Chem. Phys.* **19**, 6264 (2017).
- ²⁷L. Weston, L. Bjaalie, K. Krishnaswamy, and C. G. Van de Walle, *Phys. Rev. B* **97**, 054112 (2018).